

Multistable monochromatic laser solitons

P. Genevet, L. Columbo, S. Barland, M. Giudici, L. Gil, and J. R. Tredicce

Université de Nice Sophia Antipolis, Institut Non-Linéaire de Nice, UMR 6618, F-06560 Valbonne, France

(Received 27 January 2010; published 21 May 2010)

We study the spectral properties of stationary laser solitons (LSs) generated in two broad-area vertical cavity surface emitting lasers coupled to each other in face-to-face configuration [P. Genevet *et al.*, *Phys. Rev. Lett.* **101**, 123905 (2008)]. We demonstrate experimentally that LS emission occurs on a single longitudinal mode frequency of the compound cavity. Multistability is reported among differently “colored” LSs. We also develop a theoretical model beyond the single longitudinal mode approximation whose numerical simulation results are in good agreement with the experimental observations.

DOI: [10.1103/PhysRevA.81.053839](https://doi.org/10.1103/PhysRevA.81.053839)

PACS number(s): 42.65.Tg, 42.55.Px, 42.65.Pc, 42.79.Ta

I. INTRODUCTION

The formation of localized structures in spatially extended nonlinear systems is a broad research area that has attracted much attention during the last decades. In optics, localized structures forming in laser cavities have been cavity solitons (CSs). CSs can be independently addressed and positioned, which makes them very attractive for applications in the field of information storage and processing [1]. After the prediction of their existence in two-level feedback systems [2,3], in Kerr cavities [1], and in semiconductor microresonators [4,5], CSs were experimentally demonstrated in a broad-area vertical cavity surface emitting laser (VCSEL) coherently driven by an injected electromagnetic field [6]. CS properties have been extensively explored experimentally together with the possibility of realizing prototypical devices for information processing based on CS operations [7,8].

More recently, a new system capable of generating CS without the need of an external injection beam, called a cavity-soliton laser (CSL), has been conceived. In this system the optical bistability, which represents a favorable condition for the CS existence, is provided either by submitting a broad-area VCSEL to a frequency selective feedback [9,10] or by coupling a broad-area VCSEL to a saturable absorber. This second approach has been proposed theoretically a long time ago by N. N. Rosanov and his collaborators [11–13] in the limiting case of infinitely fast material. The authors named the bistable localized structures observed laser solitons (LSs). In the following we will therefore use equally the terms CSs and LSs to refer to these localized laser structures. Further improvements to the Rosanov model made it possible to take into account finite carrier relaxation rates and, more recently, to better describe the case of a semiconductor laser with saturable absorber [14,15]. Inspired by these theoretical results, we have recently realized experimentally a CSL by coupling two broad-area VCSELs through a self-imaging cavity [16]. While one VCSEL is operated in the amplifying regime, the second is kept under transparency and behaves as a saturable absorber. This compound cavity configuration is intrinsically longitudinally multimode since the distance L_c between the two VCSELs is of the order of 30 cm, which corresponds to an intermode spacing of ~ 500 MHz, by far smaller than the width of the semiconductor gain curve. On the other hand, the models cited previously describing CS generation in lasers with saturable absorbers have been

derived by assuming a uniform field profile in the propagation direction. This approximation is verified inside each VCSEL, where both high mirror reflectivity and single longitudinal mode operation are fulfilled, but it is no more valid when two VCSELs are coupled, forming a compound cavity. In order to better understand our experimental results, we have derived a model able to describe the intrinsic multi longitudinal mode character of our configuration.

In this article we report on the spectral properties of LSs. We first show that, although several spatial Fourier modes are required to describe the LS transverse profile, only a single well-defined temporal frequency is involved in the dynamical behavior. Even more, we observe that this frequency corresponds to a single longitudinal compound cavity mode. We also show that different monochromatic LSs can coexist for the same range of parameters and that several colors are successively selected along the hysteresis loop between the “on” and “off” laser regimes. Following the theoretical approach developed for the description of the VCSEL with injection [5], we have derived a mathematical model able to go beyond the single longitudinal mode approximation. The model is a second-order Taylor expansion in the transmission coefficient of the VCSEL mirrors (which is usually very small). A linear change of variable which mixes the electric field inside each VCSEL with the delayed electric field coming from the other VCSEL allows for a striking simplification of the dynamics. Hence, although our model contains a delay term, it has absolutely no relationship with a Lang-Kobayashi type of description since our regime of parameter is precisely opposite to the regime of validity of this approximation. The numerical simulations are in good qualitative agreement with the experimental observations.

In Sec. II we describe the experimental setup and two different experimental techniques used to measure the LS modal behavior; Sec. III is devoted to the introduction of the theoretical model and to the results of numerical simulations. Finally, in Sec. IV we draw our conclusions.

II. EXPERIMENT**A. Experimental setup**

The schematic of a CSL is presented in Fig. 1. It is basically the same experimental scheme as in [16], except for the Mach-Zehnder interferometer present on the L_2 output detection

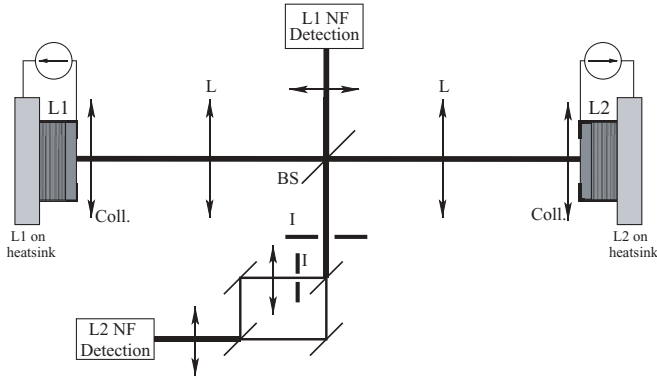


FIG. 1. Schematic of the experiment. L_1 (L_2) amplifier (absorber) semiconductor resonator; Coll, collimator; BS, beam splitter; L, lens; I, iris. The L_1 (L_2) near-field (NF) detection is composed of a CCD camera and a fast detector. Lens configuration is such that the compound cavity is self-imaging.

path. Two identical broad-area VCSELs face each other, delimiting a compound cavity which is self-imaging, thus preserving the high Fresnel number required for CS existence [17]. As already pointed out in the Introduction, the key element of this compound system is the presence of saturable absorption that provides bistability. This can be obtained by biasing one VCSEL (L_1) in the amplifying regime while keeping the second (L_2) in the absorber regime. The system parameters are set in the region where LS are stable and stationary. A detailed description of the parameter space and LS existence conditions can be found in [18].

For detection purposes, a 20% beam splitter is inserted in the CSL, making it possible to extract two output beams. The output near-field profile of L_1 is imaged on a charge-coupled CCD camera. An example of this profile containing four LSs is shown in Fig. 2.

The general method of detecting the phase profile of an electromagnetic beam is based on interference between the electromagnetic beam and a reference coherent plane wave. This reference beam can be obtained in our system by selecting a pointlike region of the output beam characterized by a stationary and coherent emission. This local beam is then

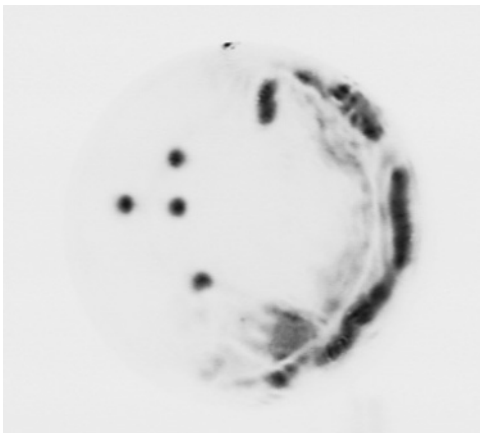


FIG. 2. Example of L_1 near-field intensity distribution. The four dark spots are laser solitons. The darker zones represent higher intensities.

expanded to a collimated waist larger than the global output beam waist of the system. This reference beam is obtained in one arm of the Mach-Zehnder interferometer placed on the detection path of the L_2 output. An iris selects the proper region of the output beam to be used as reference beam, while a lens resizes the local output beam selected. This reference beam interferes with the total output beam emitted by L_2 traveling in the other arm of the interferometer. The resulting interference patterns are imaged onto the CCD camera and correspond to the near-field phase profile of L_2 emission. Since we are interested in monitoring the spectral properties of a single LS, an iris placed before the interferometer selects only a limited spatial region (with $10 \mu\text{m}$ diameter) around the considered LS. As a matter of fact, LS phase profiles are obtained by making self-interference between the LS and a reference beam obtained from its peak. The interferometric signal, obtained by integrating the phase profile distribution in the previously described area around the LS, is useful for disclosing mode hopping of the LS, as is shown later in this article. This interferometric signal is detected by a large-area photodiode.

B. Multistable laser solitons

In [18] we demonstrated that the CS in Fig. 2 can be interpreted as independent micro-lasers since their formation is accompanied by the appearance of well pronounced peaks in the optical spectrum. Because the gain curve of semiconductor laser is very broad (some nm) compared to the free spectral range ($\Delta\nu$) of the compound cavity (in the case considered here, $\Delta\nu$ is 460 MHz), a large number of longitudinal modes can lase. As a consequence, each soliton laser can emit on a different frequency, corresponding to a different longitudinal cavity mode. In the following, we will focus our attention to the optical spectrum associated to a LS emission. Since the optical spectrum analyzer used in [18] is unable to resolve frequency separations of the order of half a GHz, we will acquire LS optical spectra by using a heterodyne technique, where a reference beam is provided by an external laser source which is tunable and frequency stabilized (linewidth smaller than 1 MHz).

1. Heterodyne measurement

The CS output beam and the reference signal are combined and sent to an 8-GHz Thorlabs PDA8GS photodetector. The beating signal is detected, amplified, and then sent into a Hewlett Packard 8593 power spectrum analyzer.

Figure 3 shows two different realizations of the recorded beating signal. The two curves have been obtained by slightly changing in the pumping current (about 0.2 mA). In this current interval LSs coexist with the homogeneous zero solution. For each curve, there is a single peak whose linewidth is of the order of few MHz. This is a clear indication that the LS is emitting on a single frequency. The main difference between the two curves is that the two peaks are separated by 460 MHz, which corresponds to the $\Delta\nu$ of the compound cavity. When the current is continuously increased, the beat peak remains single but undergoes consecutive sudden jumps of equal frequency interval. We observe that the peak jumps in the power spectrum are accompanied by modification of

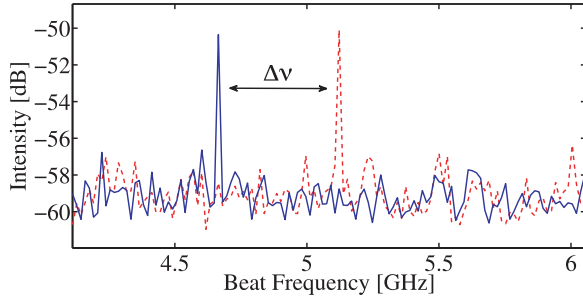


FIG. 3. (Color online) Heterodyne measurement of the laser soliton emission frequency. The continuous blue curve is obtained for a parameters set corresponding to region C of Fig. 6. The dashed red curve is obtained almost in the same regime as the first one, upon a variation of about 0.2 mA of the pumping current value. The plot clearly indicates that the emission frequency is monochromatic and that it can change only by discrete jump of one $\Delta\nu$.

the near-field phase profile detected at the output of the Mach-Zehnder interferometer.

2. Interferometric measurement

Whereas the heterodyne measurement shows the monochromaticity of the LS emission, the intensity at the output of the Mach-Zehnder interferometer could be used to detect the phase profile and the intensity profile (if the reference beam arm of the interferometer is blocked) of a single LS. Moreover, a longitudinal mode switching of a LS, for example, a jump from ω_n to $\omega_{n+1} = \omega_n + \frac{\pi c}{L_c}$, can be disclosed, monitoring the CS interferometric signal intensity. Indeed, the length difference between the interferometer arms is about $\Delta L = |L_1 - L_2| \sim 5$ cm. Therefore, the phase difference between the two beams oscillating at ω_n (ω_{n+1}) at the end of interferometer is given by $\Delta\phi_n = \frac{\omega_n \Delta L}{c}$ ($\Delta\phi_{n+1} = \frac{\omega_{n+1} \Delta L}{c}$). Since the reference beam is obtained from the monitored LS, the variation of the phase difference associated with a jump of one compound cavity mode of the LS frequency is given by

$$\Delta\phi_{n+1} - \Delta\phi_n = \pi \frac{\Delta L}{L_c} \simeq 0.15\pi \quad (1)$$

large enough to give rise to detectable variation of the interferometric signal intensity but also small enough to prevent aliasing complications. Figure 4 shows, as a function of I_1 , the interferometric signal of a LS obtained by spatial integration of the LS near-field phase profile. These phase profiles are also shown in Fig. 4. The region monitored is centered on the LS peak and has a diameter of $10 \mu\text{m}$. The existence range of the monitored LS in terms of I_1 is approximately between 250 and 255.5 mA (the reason for the word ‘‘approximately’’ in the previous sentence will be clarified in the next section). Figure 4 shows the mode hopping of the LS as a function of an upward and downward scanning of I_1 . We start to record the interferometric intensity for I_1 around 254.3 mA. For increasing I_1 (continuous red lines) from 254.5 to 256.2 mA, the interference intensity varies smoothly, indicating that the emission frequency is slightly continuously changed. This behavior can be attributed to the redshift of the cavity resonance of L_1 due to the Joule heating of

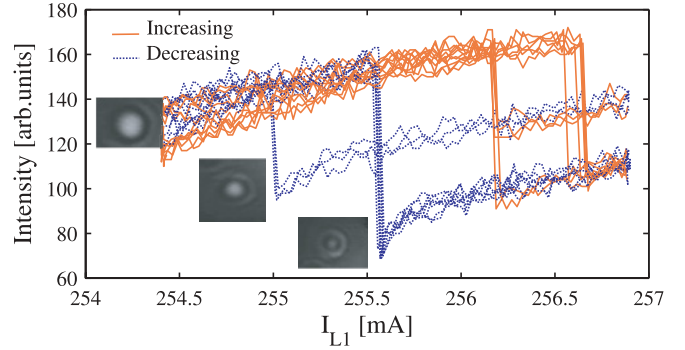


FIG. 4. (Color online) Interferometric intensity signal of a LS as a function of I_1 . The interferometric intensity signal is obtained by integrating the phase profile of the monitored LS. The dashed blue traces correspond to decreasing values of I_1 , while continuous red traces correspond to increasing values of I_1 . Variation of the interferometric intensity signal corresponds to a mode hopping of the LS. The figure shows the multistability of the CS emission frequency. The phase profiles corresponding to each branch of the hysteresis loop are shown in the insets. The spatial region monitored is centered on the LS considered and has a diameter of $10 \mu\text{m}$. Bright zones represent high intensities.

the semiconductor medium, and it is quantitatively compatible with the dependence $\frac{d\lambda}{dT}$ experimentally measured in [18]. When I_1 reaches 256.2 mA, the interferometric intensity jumps to a lower level. While the sudden jump is due to the switching of CS’s emission frequency, the fact that the intensity is lower is completely governed by the interference condition at the interferometer output. When I_1 is decreased from high current values (dashed blue lines), the interferometric intensity does not necessary jump back to the previous state for the same I_1 values. This hysteresis behavior is characteristic of a bistable regime. For $255.5 < I_1 < 256.7$ mA, there are three different possible emission frequencies that are stable simultaneously. For each emission frequency we show in Fig. 4 the corresponding phase profiles. The LS phase profiles shows a concentric intensity pattern with different output intensity level that are attributed to different emission frequencies of the LS. The concentric shape of the equiphase lines are attributed to the radial phase distribution of the LS (which has been also found theoretically in [13]). We notice that the measurement performed above was obtained by scanning all the way up and all the way down the pumping current. Even if this method makes it possible to check the multistability of the CS emission frequency, the full study of the stability of each branch requires repeating the upward and downward scanning of the parameter starting for each branch.

C. CS switch-off

Figure 5 shows the LS intensity output when I_1 is scanned on the whole cycle of bistability of the considered LS, from the homogeneous solution to the upper state. The LS intensity output is obtained from integration of the output from a $10\text{-}\mu\text{m}$ -diameter region centered on a LS peak. This figure, obtained when the reference arm of the interferometer is blocked, shows the typical hysteresis cycle of a LS, which is bistable for $245 < I_1 < 249$ mA. The intensity emitted in

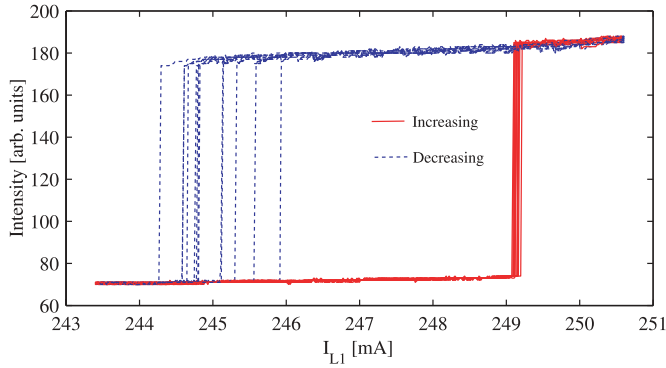


FIG. 5. (Color online) Intensity output of a LS as a function of I_1 . The intensity output is obtained by integrating its emission on a $10\text{-}\mu\text{m}$ -diameter region centered on its peak. This can be obtained easily using the same setup used for Fig. 4 by blocking an interferometer arm, avoiding interference. The red trace indicates increasing I_1 values. The dashed blue trace indicates decreasing I_1 values. The considered LS is bistable for $245 < I_1 < 249$ mA.

the upper state is almost constant along the whole stability branch. We note the wide dispersion of the switch-off current values compared to the switch-on ones. To understand the reason for this large dispersion, we perform the same curve but using the interferometric signal, that is, opening the reference arm of the interferometer. The result is presented in Fig. 6. As previously discussed, the interferometric signal makes it possible to observe the longitudinal mode switching when the parameters are changed. The weak variation of the interferometric signal when such switching occurs (as shown in Sec. II B2) does not hide the hysteresis loop of the LS intensity. As a consequence, we can follow the LS switch-on when $I_1 > 249$ mA. Nevertheless, the interferometric intensity registered when scanning the switched-on branch of the LS exhibits sudden variations. This indicates the presence of mode hopping of the LS and therefore that the compound cavity mode on which the LS emits is not always the same. In particular, when downward scanning I_1 , we observe three different spectral behaviors of the LS. Close to the high current values (denoted by the letter C in Fig. 6), the CS is

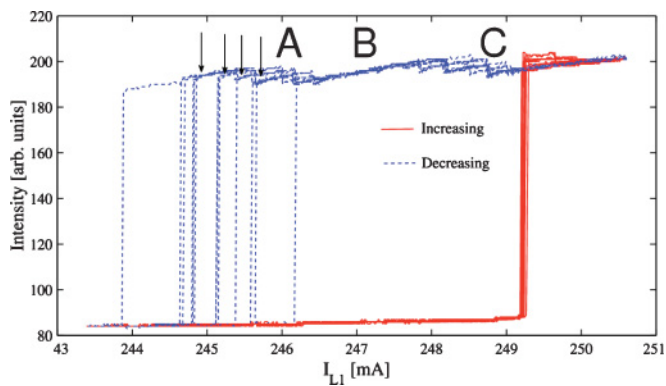


FIG. 6. (Color online) Same measurement as in Fig. 5 but with both arms of the interferometer opened, allowing for interference. We observe the mode hopping of the LS when I_1 is scanned in the LS bistable region. A corresponds to the switch-off region; B, the bistable zone; and TXtable C, the multistable zone.

spectrally multistable and can operate at different frequencies. In this regime and for a given value of I_1 , the heterodyne measurement (Fig. 3) shows random jumps that could be triggered by the noise. Incidentally, we also notice that, for current values higher than the upper bistability limit of the LS, the heterodyne measurement may reveal multi-peaks associated with a nonstationary CS amplitude. When the current is decreased, we enter a zone denoted by the letter B, which is 1 mA wide, where the LS emission frequency is almost constant. For lower current values, we observe the region denoted by the letter A, where the LS switch-off takes place. The usual mechanism involved in the switch-off of a laser with saturable absorber is the following: When the pump current is decreased the lasing operation persists until the intracavity field is too weak to sustain the saturation. In our case, the interferometric measurement highlights a specific LS switch-off behavior. We observe that the wide dispersion in the switch-off current values is due to the LS spectral properties. If the current is decreased from region B, the LS can disappear because the amplitude of the intracavity field associated with its emission frequency is not sufficient to sustain saturation or it can jump to a different frequency branch corresponding to a higher amplitude. In the latter case, the LS can remain switched on but it operates at a new frequency. If we continue to decrease I_1 , the LS may continue to stay on by multiplying these hops to different compound cavity modes, as shown in Fig. 6. Whether the LS switches off or optimizes its frequency, staying alive with decreasing I_1 , depends on the realization, and different loops give different LS switch-off values of I_1 . The switching-off process happens therefore for a set of discrete current values denoted by the black arrows in Fig. 6.

In Fig. 7 we show again the interferometric intensity as function of I_1 but only for two increasing and decreasing sweeps of I_1 . This figure illustrates clearly the possibility for the CS to disappear or to switch on a new longitudinal mode. For both cycles, the LS switches on for $I_1 \sim 255.5$ mA. However, when I_1 is decreased, we observe the switch-off at $I_1 \sim 251$ mA for the first cycle. While for the second cycle, when the current value reaches the edge of the stability branch of the active mode, the CS emission frequency jumps suddenly to another cavity mode able to sustain the saturation of the absorber. To see the structure disappear, the value of the

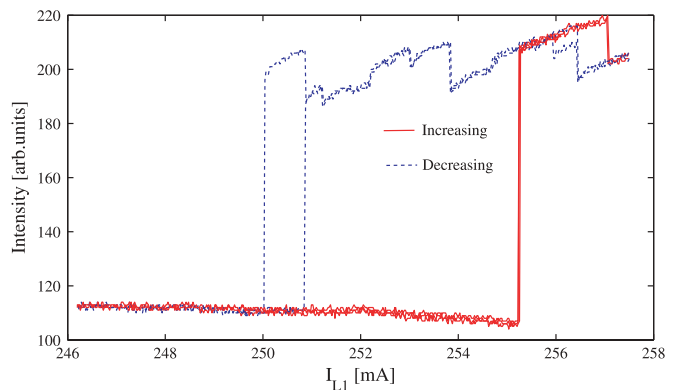


FIG. 7. (Color online) Interferometric intensity signal as function of I_1 for only two hysteresis cycles.

pumping current must be lowered down to the edge of the new mode's stability branch ($I_1 \sim 250$ mA).

III. THEORY

Theoretical models have already been developed to describe the coupling between a broad area VCSEL and a semiconductor saturable absorber [14,15]. However, these models are limited to the case of monolithic devices with a characteristic longitudinal length of $\sim 1 \mu\text{m}$, where the active and passive media are placed in the same "good" cavity (i.e., high-reflectivity resonator). In such a case, the slowly varying amplitudes of the electric field and of the induced medium polarization can be considered uniform in the propagation direction. The latter approximation is clearly not sufficient to describe the doubled cavity configuration used in [16] to realize the CSL. This consideration brought us to develop a new theoretical approach beyond the uniform field limit. We want our model to properly take into account: (i) the two different VCSELs operation regimes, (ii) the very different temporal and spatial scales involved in the composite system dynamics, and (iii) the multiple reflections at the VCSELs-air interfaces.

In the following we first derive this model and then compare the results of numerical simulations with those reported in the previous section.

We adopt the following notation (see Fig. 8) for the electric fields inside the VCSEL1 and the VCSEL2:

$$\mathcal{E}_{1,2} = \frac{1}{2} [E_{F_{1,2}} e^{i(k_0 z - \omega_0 t)} + E_{B_{1,2}} e^{i(-k_0 z - \omega_0 t)} + \text{c.c.}],$$

where z denotes the propagation direction, $E_{F,B}$ represent the slowly varying envelopes of the forward and backward fields inside the two VCSELs, $k_0 = \frac{\omega_0 n}{c}$ where n is the background refractive index, and ω_0 is a reference frequency close to the maximum of the semiconductor gain curve. We choose ω_0 as one of the VCSEL's empty cavity resonances. Indeed, VCSELs are usually designed in order to display the lowest pumping threshold and this condition is achieved when the maximum gain curve coincides with an empty cavity resonance. Finally, the difference between the previous frequency and the one which is effectively selected at threshold is proportional to $|T|^2$, where T is the transmission coefficient of the VCSEL Bragg mirrors ($|T| \ll 1$).

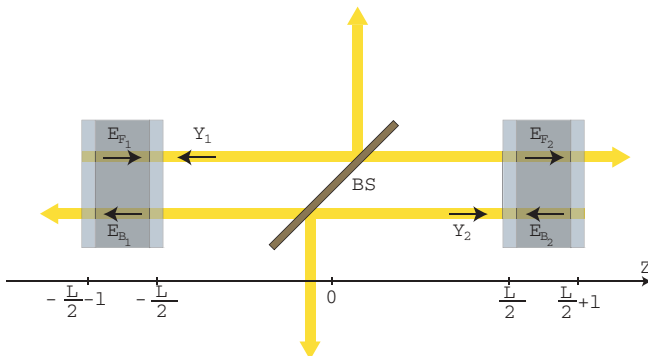


FIG. 8. (Color online)

The amplitudes of the fields and of the medium polarizations $P_{F,B}$ inside VCSEL1 (working as amplifier) obey a set of effective Maxwell-Bloch equations [19,20]:

$$\begin{aligned} \frac{n_g}{c} \frac{\partial E_{F_1}}{\partial t} &= \frac{i\omega_0 \Gamma_c}{2\epsilon_0 n c} P_{F_1} - \frac{\partial E_{F_1}}{\partial z} + \frac{i}{2k_0} \nabla_{\perp}^2 E_{F_1}, \\ \frac{n_g}{c} \frac{\partial E_{B_1}}{\partial t} &= \frac{i\omega_0 \Gamma_c}{2\epsilon_0 n c} P_{B_1} + \frac{\partial E_{B_1}}{\partial z} + \frac{i}{2k_0} \nabla_{\perp}^2 E_{B_1}, \\ \frac{\partial P_{F_1}}{\partial t} &= \frac{\Gamma(N_1)(1 - i\alpha) + 2i\delta(N_1)}{\tau_d} \\ &\quad \times [-f_0 \epsilon_0 n^2 (\alpha + i)(N_1/N_0 - 1)E_{F_1} - P_{F_1}], \\ \frac{\partial P_{B_1}}{\partial t} &= \frac{\Gamma(N_1)(1 - i\alpha) + 2i\delta(N_1)}{\tau_d} \\ &\quad \times [-f_0 \epsilon_0 n^2 (\alpha + i)(N_1/N_0 - 1)E_{B_1} - P_{B_1}]. \end{aligned}$$

In the preceding equations, n_g is the group index ($c \frac{dk}{d\omega}$); the confinement factor is given by $\Gamma_c = \frac{l_a}{l}$, where l_a represents the length of active medium; $\alpha \in \mathcal{R}$ is the linewidth enhancement factor; N_0 is the value of carrier density at transparency; f_0 is a real constant; and τ_d is the microscopic dipole dephasing time. $\Gamma = \bar{\Gamma}_0 + \bar{\Gamma}_1 N/N_0$ and $\delta = \bar{\delta}_0 + \bar{\delta}_1 N/N_0$ are real functions of the carrier density. The parameters N_0 , f_0 , α , $\bar{\Gamma}_0$, $\bar{\Gamma}_1$, $\bar{\delta}_0$, and $\bar{\delta}_1$ are derived by the fit of the semiconductor susceptibility for a GaAs/Al_{0.2}Ga_{0.8} quantum well calculated from microscopic theory [19,20].

The equation for the carrier density N_1 reads [21]

$$\begin{aligned} \frac{\partial N_1}{\partial t} &= -\frac{1}{\tau_{\parallel}} N_1 + I_1 + d \nabla_{\perp}^2 N_1 \\ &\quad - \frac{i}{4\hbar} (E_{F_1}^* P_{F_1} - E_{F_1} P_{F_1}^* + E_{B_1}^* P_{B_1} - E_{B_1} P_{B_1}^*), \end{aligned}$$

where τ_{\parallel} is the nonradiative decay time, I_1 is the pump parameter, and d is the carrier diffusion coefficient.

Since VCSEL2 is supposed to be under transparency and then driven by VCSEL1, we may adiabatically eliminate the polarization equation without inducing any unphysical spatial instability. Note that this approach has previously been successfully used to describe CS in driven VCSEL [5]. It leads to

$$\begin{aligned} \frac{n_g}{c} \frac{\partial E_{F_2}}{\partial t} &= \frac{i\omega_0 \Gamma_c}{2nc} \chi_p E_{F_2} - \frac{\partial E_{F_2}}{\partial z} + \frac{i}{2k_0} \nabla_{\perp}^2 E_{F_2}, \\ \frac{n_g}{c} \frac{\partial E_{B_2}}{\partial t} &= \frac{i\omega_0 \Gamma_c}{2nc} \chi_p E_{B_2} + \frac{\partial E_{B_2}}{\partial z} + \frac{i}{2k_0} \nabla_{\perp}^2 E_{B_2}, \\ \frac{\partial N_2}{\partial t} &= -\frac{1}{\tau_{\parallel}} N_2 + I_2 + \frac{\epsilon_0 \text{Im}(\chi_p)}{2\hbar} (|E_{F_2}|^2 + |E_{B_2}|^2) \\ &\quad + d \nabla_{\perp}^2 N_2, \end{aligned}$$

with $\chi_p = -\frac{nc}{\omega_0} \Theta \tilde{A} (N_2 - N_0)$, where \tilde{A} is a differential absorption coefficient (having dimension of length squared); $\Theta = \frac{\Delta + i}{1 + \Delta^2}$ and $\Delta = (\omega_e - \omega_0)/\gamma_e$, where ω_e is the central frequency of the excitonic absorption line, approximated by the Lorentzian shape; and γ_e is its half-width.

To deal with adimensional quantities, we introduce the new variables

$$E'_{F_{1,2}, B_{1,2}} = \eta_1 E_{F_{1,2}, B_{1,2}}, \quad P'_{F_1, B_1} = \eta_2 P_{F_1, B_1},$$

$$N'_{1,2} = \left(\frac{N_{1,2}}{N_0} - 1 \right), \quad \partial_{t'} = \tau_d \partial_t, \quad \nabla_{\perp}^{\prime 2} = \frac{c\tau_d}{2n_g k_0} \nabla_{\perp}^2,$$

where $\eta_1 = -if_0 \epsilon_0 n^2 \eta_2$ and $|\eta_2|^2 = \tau_{\parallel} / \hbar N_0 f_0 \epsilon_0 n^2$.

Dropping the primes we then have:

$$\begin{aligned} \partial_t E_{F_1} &= \rho P_{F_1} - \frac{c\tau_d}{n_g} \partial_z E_{F_1} + i \nabla_{\perp}^2 E_{F_1}, \\ \partial_t E_{B_1} &= \rho P_{B_1} + \frac{c\tau_d}{n_g} \partial_z E_{B_1} + i \nabla_{\perp}^2 E_{B_1}, \\ \partial_t P_{F_1} &= [\Gamma(1 - i\alpha) + 2i\delta] [(1 - i\alpha)N_1 E_{F_1} - P_{F_1}], \\ \partial_t P_{B_1} &= [\Gamma(1 - i\alpha) + 2i\delta] [(1 - i\alpha)N_1 E_{B_1} - P_{B_1}], \\ \partial_t N_1 &= b \left[-N_1 + \mu_1 + D \nabla_{\perp}^2 N_1 - 1/4 (\overline{E_{F_1}} P_{F_1} + E_{F_1} \overline{P_{F_1}} \right. \\ &\quad \left. + \overline{E_{B_1}} P_{B_1} + E_{B_1} \overline{P_{B_1}}) \right] \end{aligned} \quad (2)$$

and

$$\begin{aligned} \partial_t E_{F_2} &= \rho C (-i\Theta) N_2 E_{F_2} - \frac{c\tau_d}{n_g} \partial_z E_{F_2} + i \nabla_{\perp}^2 E_{F_2}, \\ \partial_t E_{B_2} &= \rho C (-i\Theta) N_2 E_{B_2} + \frac{c\tau_d}{n_g} \partial_z E_{B_2} + i \nabla_{\perp}^2 E_{B_2}, \\ \partial_t N_2 &= b \left[-N_2 + \mu_2 + D \nabla_{\perp}^2 N_2 - \frac{C}{2(1 + \Delta^2)} N_2 (|E_{F_2}|^2 \right. \\ &\quad \left. + |E_{B_2}|^2) \right], \end{aligned} \quad (3)$$

where

$$\rho = \frac{\omega_0 \Gamma_c \tau_d f_0 n}{2n_g}, \quad D = \frac{2n_g k_0 \tau_{\parallel}}{c\tau_d} d, \quad b = \frac{\tau_d}{\tau_{\parallel}},$$

$$\mu_{1,2} = \frac{\tau_{\parallel} I_{1,2}}{N_0} - 1, \quad C = \frac{c \tilde{A} N_0}{\omega_0 f_0 n}.$$

The longitudinal coordinate z is purposely not involved in the scalings.

Using the adimensional variables, boundary conditions are expressed as

$$\begin{aligned} E_{F_1} \left(z = -\frac{L}{2} - l \right) &= R E_{B_1} \left(z = -\frac{L}{2} - l \right) e^{i2k_0(\frac{L}{2} + l)}, \\ E_{B_1} \left(z = -\frac{L}{2} \right) &= R E_{F_1} \left(z = -\frac{L}{2} \right) e^{-2ik_0 \frac{L}{2}} \\ &\quad + T \gamma_1 Y_1 \left(z = -\frac{L}{2} \right), \\ E_{F_2} \left(z = +\frac{L}{2} \right) &= R E_{B_2} \left(z = +\frac{L}{2} \right) e^{-i2k_0 \frac{L}{2}} \\ &\quad + T \gamma_1 Y_2 \left(z = +\frac{L}{2} \right), \\ E_{B_2} \left(z = +\frac{L}{2} + l \right) &= R E_{F_2} \left(z = +\frac{L}{2} + l \right) e^{i2k_0(\frac{L}{2} + l)}, \end{aligned} \quad (4)$$

where $Y_{1,2}$ represent the amplitudes of the adimensional fields incident respectively on the VCSEL1 and VCSEL2 and the parameter γ_l stands for the linear losses in the space between the two VCSELs. The effective reflection coefficient R and transmission coefficient T , complex quantities in the general case, satisfy the relation $|R|^2 + |T|^2 = 1$.

It is convenient at this point to introduce the following linear change of variables:

$$\begin{aligned} E'_{F_1}(t, x, z) &= \eta_{F_1} e^{+(z+L/2+l)\frac{\log(R)}{l}} E_{F_1}(t, x, z) \\ &\quad + (a_1 + b_1 z) Y_1(t, x, -L/2), \\ P'_{F_1}(t, x, z) &= \eta_{F_1} e^{+(z+L/2+l)\frac{\log(R)}{l}} P_{F_1}(t, x, z), \\ E'_{B_1}(t, x, z) &= \eta_{B_1} e^{-(z+L/2)\frac{\log(R)}{l}} E_{B_1}(t, x, z) \\ &\quad + (c_1 + d_1 z) Y_1(t, x, -L/2), \\ P'_{B_1}(t, x, z) &= \eta_{B_1} e^{-(z+L/2)\frac{\log(R)}{l}} P_{B_1}(t, x, z), \\ E'_{F_2}(t, x, z) &= \eta_{F_2} e^{+(z-L/2)\frac{\log(R)}{l}} E_{F_2}(t, x, z) \\ &\quad + (a_2 + b_2 z) Y_2(t, x, L/2), \\ E'_{B_2}(t, x, z) &= \eta_{B_2} e^{-(z-L/2-l)\frac{\log(R)}{l}} E_{B_2}(t, x, z) \\ &\quad + (c_2 + d_2 z) Y_2(t, x, L/2), \end{aligned}$$

where $\eta_{F_{1,2}}, \eta_{B_{1,2}}, a_{1,2}, b_{1,2}, c_{1,2}$, and $d_{1,2}$ are complex constants that we choose such that (i) the new field variables satisfy ideal mirror boundary conditions,

$$\begin{aligned} E'_{F_1} \left(z = -\frac{L}{2} \right) &= E'_{B_1} \left(z = -\frac{L}{2} \right), \\ E'_{F_1} \left(z = -l - \frac{L}{2} \right) &= E'_{B_1} \left(z = -l - \frac{L}{2} \right), \\ E'_{F_2} \left(z = l + \frac{L}{2} \right) &= E'_{B_2} \left(z = l + \frac{L}{2} \right), \\ E'_{F_2} \left(z = \frac{L}{2} \right) &= E'_{B_2} \left(z = \frac{L}{2} \right), \end{aligned}$$

and (ii) Eqs. (2) and (3) can be more simply rewritten. Because a detailed description of the electric field and polarization inside each VCSEL is not of strong interest, we also perform an integration over the length z of each VCSEL in order to deal only with their average value.

To complete the model, we have to take into account that in the experimental configuration, the temperature of each VCSEL is independently controlled, leading to a possible detuning between the two VCSEL cavity resonances. Experimentally, this thermally mediated detuning turns out to be crucial, with a critical sensitivity of the output intensities on the controlled temperature of each VCSEL. We model this possibility with the introduction of the additional parameter ϕ . Also, we find it convenient to define the new parameter $\xi = \frac{\tau_d c}{2n_g l}$. Finally, forgetting the prime notation, we obtain

$$\begin{aligned} \partial_t E_1(t, x) &= -\xi |T|^2 E_1(t, x) + \rho P_1(t, x) + i \nabla_{\perp}^2 E_1(t, x) \\ &\quad - \gamma_1 \xi |T|^2 e^{ik_0 L} E_2(t - \tau, x), \\ \partial_t E_2(t, x) &= i\phi E_2(t, x) - \xi |T|^2 E_2(t, x) + i \nabla_{\perp}^2 E_2(t, x) - i\Theta \rho \\ &\quad \times C N_2(t, x) E_2(t, x) - \gamma_1 \xi |T|^2 e^{ik_0 L} E_1(t - \tau, x), \\ \partial_t P_1(t, x) &= [\Gamma(N_1)(1 - i\alpha) + 2i\delta(N_1)] \\ &\quad \times [E_1(t, x) N_1(t, x)(1 - i\alpha) - P_1(t, x)], \end{aligned}$$

$$\begin{aligned}
 \partial_t N_1(t,x) &= b \left[-N_1(t,x) + \mu_1 + D\nabla_{\perp}^2 N_1(t,x) \right. \\
 &\quad \left. - \frac{1}{8}(\overline{E_1} P_1 + E_1 \overline{P_1}) \right], \\
 \partial_t N_2(t,x) &= b \left\{ -N_2(t,x) + \mu_2 + D\nabla_{\perp}^2 N_2(t,x) \right. \\
 &\quad \left. - \frac{CN_2(t,x)}{4(1+\Delta^2)} \left[|E_2(t,x)|^2 + \frac{\gamma_l^2}{3} |E_1(t-\tau,x)|^2 \right] \right\}
 \end{aligned} \tag{5}$$

We made the following choice for the physical parameters in the model [5,19,20]: $\omega_0 = 2.3 \times 10^{15}$ Hz, $N_0 = 1.167 \times 10^{24} \text{ m}^{-3}$, $f_0 = \frac{c}{n\omega_0} \times 2.75 \times 10^5 \text{ m}^{-1}$, $\alpha = 3$, $\Gamma(N_1) = 0.276 + 1.016N_1$, $\delta(N_1) = -0.169 + 0.216N_1$, $n = 3.5$, $n_g = 4.6$, $l = 1 \mu\text{m}$, $l_a = 110 \text{ nm}$, $\tau_d = 300 \text{ fs}$, $D = 2.74$, $b = 10^{-4}$, $\Delta = -0.92$, $C = 50$, $|T|^2 = 4 \times 10^{-3}$. We then also have: $\xi = 10$ and $\rho = 3 \times 10^{-2}$.

For the cavity length which is used experimentally, the delay τ is about $\simeq 4000$ in rescaled time units. However, the numerical simulations of (5) with such a long delay requires an amount of memory which exceeds our computer capacity. Also from a practical point of view, possible industrial applications are interested in small external cavities and not in large ones. Therefore, in what follows, we will limit ourselves to $\tau = 1000$ (except for Fig. 13, for which $\tau = 100$). Nevertheless, because our results are in very good agreement with the experimental observations, we believe that this restriction does not matter, at least for a qualitative point of view.

The system (5) represents a set of delayed nonlinear partial differential equations that can be solved only numerically. Although it looks like the well-known Lang-Kobayashi delay differential equation model [22], our system has been derived in exactly the opposite limit $T \rightarrow 0$, fully experimentally justified.

A. Continuous-wave solutions

We look for homogenous single-frequency solutions of Eq. (5) [also named continuous-wave (cw) solutions], in the form

$$\begin{aligned}
 E_1(t) &= E_{1s} e^{i\omega t}, \quad P_1(t) = P_{1s} e^{i\omega t}, \quad N_1 = N_{1s}, \\
 E_2(t) &= E_{2s} e^{i\omega t}, \quad N_2 = N_{2s}.
 \end{aligned} \tag{6}$$

We get:

$$\begin{aligned}
 0 &= -E_{1s}(\xi|T|^2 + i\omega) + \rho P_{1s} - \gamma_l \xi |T|^2 E_{2s} e^{i(k_0 L - \omega\tau)}, \\
 0 &= -E_{2s}(\xi|T|^2 + i\omega - \phi) - i\theta \rho C N_{2s} E_{2s} \\
 &\quad - \gamma_l \xi |T|^2 E_{1s} e^{i(k_0 L - \omega\tau)}, \\
 P_{1s} &= \frac{N_{1s} E_{1s} (1 - i\alpha)(\Gamma - i\Gamma\alpha + 2i\delta)}{(\Gamma - i\Gamma\alpha + 2i\delta + i\omega)}, \\
 N_{1s} &= \frac{\mu_1}{1 + \mathcal{A}|E_{1s}|^2}, \\
 N_{2s} &= \frac{\mu_2}{1 + \frac{C}{2(1+\Delta^2)} \left(\frac{1}{2}|E_{2s}|^2 + \frac{1}{6}\gamma_l^2 |E_{1s}|^2 \right)},
 \end{aligned} \tag{7}$$

with the auxiliary quantity \mathcal{A} given by

$$\mathcal{A} = \text{Re} \left[\frac{(1 - i\alpha)(\Gamma - i\Gamma\alpha + 2i\delta)}{4(\Gamma - i\Gamma\alpha + 2i\delta + i\omega)} \right],$$

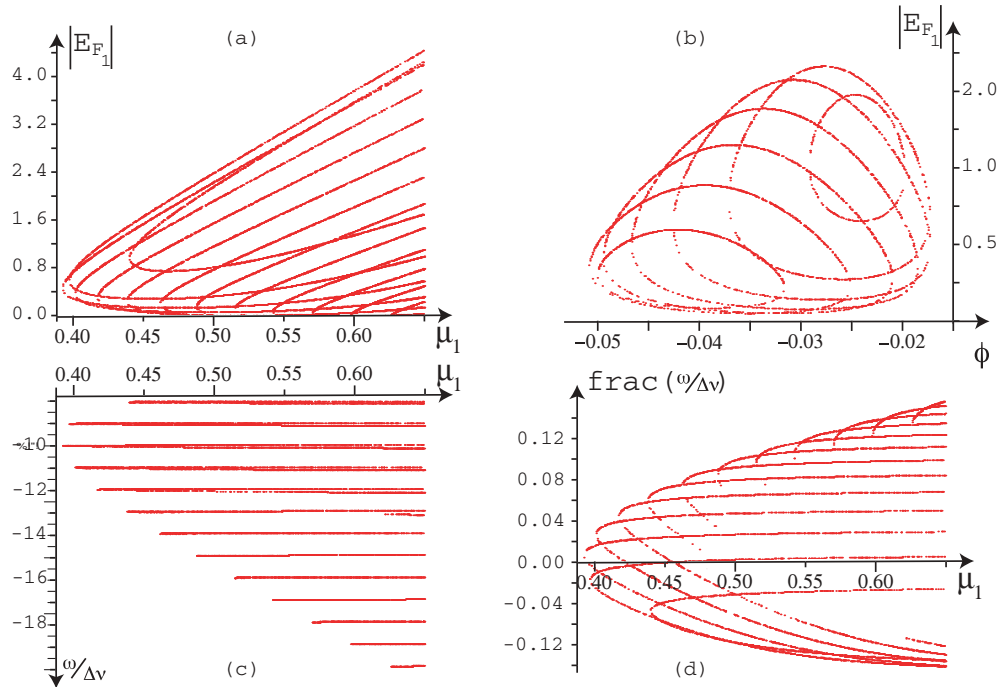


FIG. 9. (Color online) Continuous-wave solutions of Eqs. (5). Parameter set: $\mu_2 = -0.01$, $\tau = 1000$, $b = 10^{-4}$, $\xi = 10$, $\rho = 0.03$, $\alpha = 3.0$, $T = i0.0632$, $C = 50$, $\Delta = -0.92$, $k_0 L = 2m\pi$, $m \in \mathbb{Z}$, and $\gamma_l = 0.88$. Panel (b) displays $|E_1|$ versus ϕ for $\mu_1 = 0.45$. Note the strong dependence of the intensity with the detuning parameter ϕ . We select $\phi = -0.028$ and investigate the cw features. Panel (a) displays $|E_1|$ versus μ_1 , while panel (c) deals with the cw frequency ω as a function of the same parameter. Clearly, the selected frequencies are close to multiple of the $\Delta\nu$. In panel (d) we plot the distance between the selected frequency and the closest $\Delta\nu$ multiple versus μ_1 .

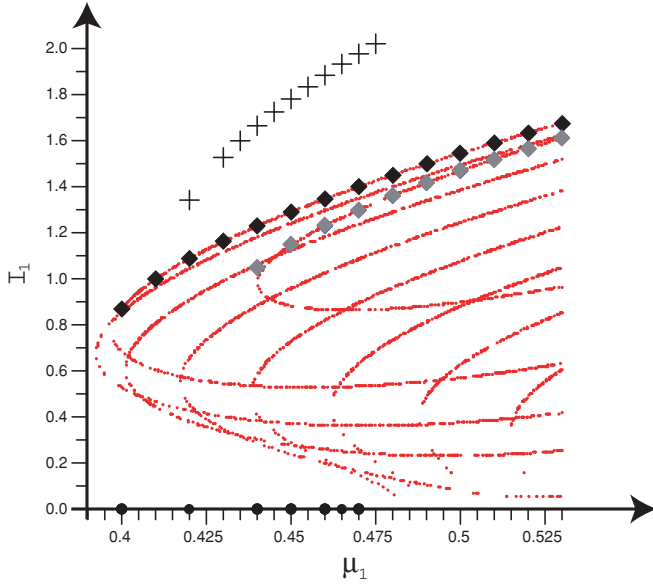


FIG. 10. (Color online) Plot of the intensity $I_1 = |E_1|$ versus μ_1 . The regime of parameters is the same as in Fig. 9. The small points correspond to analytic predictions [same as Fig. 9(a)], while the other symbols are associated with numerical simulations of (5). Black and gray diamonds correspond to stable cw solutions of (5) without transverse space dimension. On the contrary, for the black discs (off solution) and the crosses (cavity solitons), diffraction has been taken into account. Strikingly, gray diamonds are associated with a frequency equal to $-8 \Delta\nu$, black ones to $-9 \Delta\nu$, and crosses to $-10 \Delta\nu$.

which is a strongly nonlinear system of equations that can be solved only numerically. Figure 9 deals with cw solutions but contains no information about their stability. However the main features of the system are already visible: First, there exists a range of bistability between the off and the on solutions. Second, there exists a full discrete set of cw solutions which are indexed by their frequency [Figs. 9(a) and 9(c)]. Third, the selected frequencies are close to a multiple of the $\Delta\nu$ [Figs. 9(c) and 9(d)].

The stability of the cw solutions is then numerically investigated (Fig. 10). Several remarks are in order.

(i) There is a very good agreement between the cw solutions computed with (7) and the results of the numerical simulation of (5).

(ii) Although there exist many cw solutions associated with various frequencies (Fig. 9), only those corresponding to $8 \Delta\nu$ (gray diamonds) or $9 \Delta\nu$ (black diamonds) are found to be stable with respect to homogenous perturbations (Fig. 10).

(iii) The black and gray diamonds in Fig. 10 correspond to numerical simulations of Eq. (5) without transverse space dimension. When diffraction is taken into account, these homogenous cws turn out to be unstable with respect to spatial periodic modulations (not shown).

B. Monochromatic cavity solitons

Looking for localized structures of (5) sitting on a zero-intensity background, we restrict ourselves to solutions which are invariant with respect to rotation around the z propagation

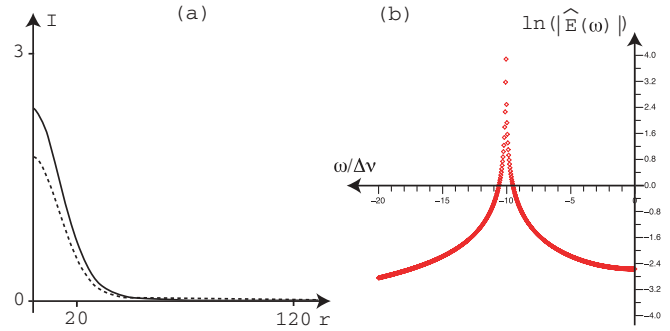


FIG. 11. (Color online) Stable monochromatic cavity soliton. The regime of parameters is the same as in Fig. 9, except $\mu_1 = 0.43$. Panel (a) displays $|E_1|$ and $|E_2|$ versus r . Panel (b) displays the power spectrum of $E_1(r=0, t)$.

axis. Then the various variables depend just on the radius r and the transverse Laplacian is reduced to

$$\nabla_{\perp}^2 = \frac{\partial^2}{\partial r^2} + \frac{1}{r} \frac{\partial}{\partial r}.$$

Also, symmetric ($r \rightarrow -r$) boundary conditions are involved for $r \rightarrow 0$ and vanishing ones for $r \rightarrow +\infty$. Following the recipe described in [14,15], we use suitable addressing pulses to locally saturate the absorption in a region of the parameter space where the laser “off” solution is stable and coexists with a nontrivial cw. The resulting self-confined laser structures sitting on a zero-intensity background have stationary amplitude and are stable over a sizable range of the control parameter μ_1 (Fig. 10). Figure 11 displays a typical plot of the intensity $|E_1|$ versus r as well as the power spectrum of $E_1(r=0, t)$. Although several transverse Fourier modes are involved in the description of the LS, only a single longitudinal frequency is observed to be brought into play by the dynamics. On the scale of the $\Delta\nu$, the LS are monochromatic.

Note that this observation is fully consistent with the analytical computation. Indeed, looking for solutions of (5) in the form

$$\begin{aligned} E_1(t) &= E_{1s} e^{i(\omega t - q_x x)}, & P_1(t) &= P_{1s} e^{i(\omega t - q_x x)}, & N_1 &= N_{1s}, \\ E_2(t) &= E_{2s} e^{i(\omega t - q_x x)}, & N_2 &= N_{2s}, \end{aligned} \quad (8)$$

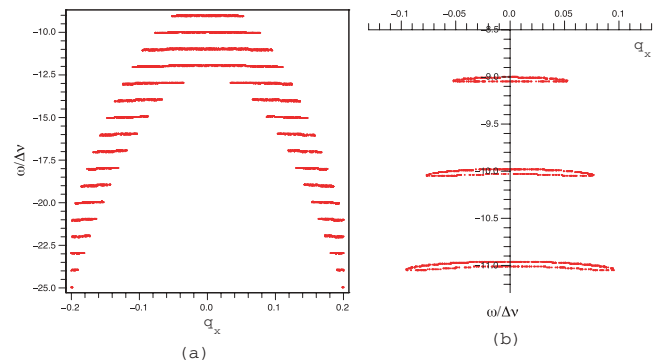


FIG. 12. (Color online) The same regime of parameter as in Fig. 11. Panel (a) displays the optical frequency ω normalized to the $\Delta\nu$ versus the transverse Fourier mode q_x . Panel (b) is an enlargement of (a) showing the tiny dependence of the frequency with q_x .

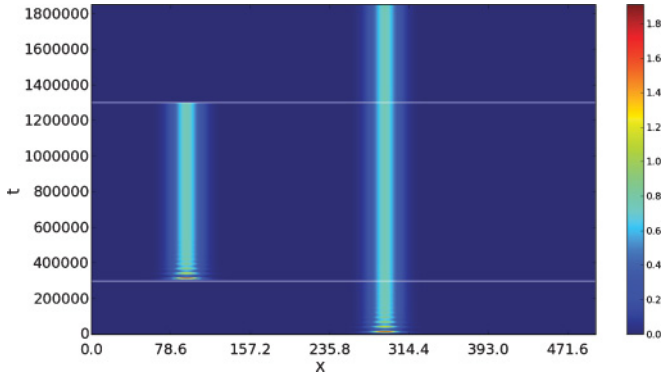


FIG. 13. (Color online) 1D numerical simulations of (5) with the same regime of parameters as in Fig. 9 except $\tau = 100$, $\mu_2 = -0.04$, $\mu_1 = 0.72$, $\phi = 0$, and $\gamma_l = 0.95$. A second LS is switched on next to an existing one by means of a second writing beam. The two LS persist after the extinction of the second injected pulse. By superimposing a high-intensity injected pulse on the second LS, it is possible to switch it “off” independently from the first.

we obtain a nonvanishing solution provided that ω and q_x obey to the dispersion relation displays in Fig. 12. In this figure, each separate branch of the dispersion relation is associated with a single longitudinal frequency. Also, the interval q_x which is associated with the same given longitudinal frequency is in agreement with the size of the LS. Indeed, for $\omega = -10\Delta\nu$, we measure $\delta q_x \simeq -0.16$, which leads to a radius $\simeq 20 (2\pi/\delta q_x)$ for the LS, in agreement with Fig. 11(a).

In order to test the CS nature (according the operative definition given, for example, in [6]) of our localized structures, we go back to 1D numerical simulation of (5), that is, $\nabla_{\perp}^2 = \partial_{xx}$. Figure 13 illustrates the possibility of independently writing and erasing a LS. Note that we used $\tau = 100$ in this simulation instead of the usual value 1000. The reason is that CSs are found to be more stable in two dimensions (2D) than their analogs in one dimension (1D). Hence, for $\tau = 1000$ CSs exist in 2D but not in 1D, while for $\tau = 100$ they exist in both space dimensions.

C. Frequency bistability

We name “frequency bistability” the possibility for a monochromatic cavity soliton, for the same given set of parameters but depending on the initial conditions, to exist with distinct frequencies (separated by a multiple of the $\Delta\nu$). This possibility has previously been reported (Fig. 7) and is also observed numerically (Fig. 14). The fact that only two frequencies are reported in the numerical simulations results

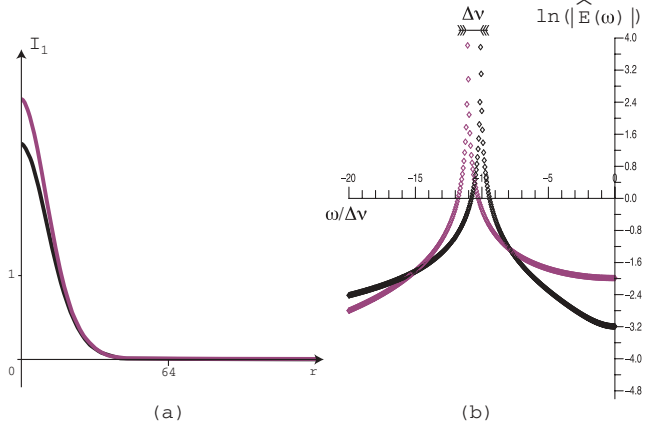


FIG. 14. (Color online) Frequency bistability: numerical simulations of (5) with $\mu_1 = 0.45$, $\phi = -0.03275$, and the other parameters are the same as in Fig. 9. Panel (a) displays the intensity $|E_1|$ versus r and panel (b) the power spectrum of $E_1(r=0, t)$. The dark and lighter lines have been obtained with the same regime of parameters; they both correspond to a stable CS but only differ by their initial conditions.

only from the small value of τ we have been forced to consider because of CPU time consideration.

IV. CONCLUSIONS

To conclude, we have proved by using complementary experimental measurements that the LS emission frequencies in a long compound cavity are multistable and that their stability domain is mainly governed by the compound modes competition. The presence of this high level of multistability could not be observed in experiments where CSs are generated in a driven microcavity because the presence of an injection field fixes the reference frequency of emission. Our theoretical model, which correctly takes into account the intrinsic multilongitudinal character of the CSL configuration, turns out to be in very good qualitative agreement with the experimental observations. Multistability, monochromatic CS, and frequency bistability are all experimental features which can be reproduced.

ACKNOWLEDGMENT

This work was supported by the FET Open Project FunFACS (www.funfacs.org).

[1] W. J. Firth and A. J. Scroggie, *Phys. Rev. Lett.* **76**, 1623 (1996).
 [2] N. N. Rosanov and G. V. Khodova, *Opt. Spectrosc.* **65**, 449 (1988).
 [3] M. Brambilla, L. A. Lugiato, and M. Stefani, *Europhys. Lett.* **34**, 109 (1996).
 [4] M. Brambilla, L. A. Lugiato, F. Prati, L. Spinelli, and W. J. Firth, *Phys. Rev. Lett.* **79**, 2042 (1997).

[5] L. Spinelli, G. Tissoni, M. Brambilla, F. Prati, and L. A. Lugiato, *Phys. Rev. A* **58**, 2542 (1998).
 [6] S. Barland *et al.*, *Nature* **419**, 699 (2002).
 [7] F. Pedaci, P. Genevet, S. Barland, M. Giudici, and J. R. Tredicce, *Appl. Phys. Lett.* **89**, 221111 (2006).
 [8] F. Pedaci *et al.*, *Appl. Phys. Lett.* **92**, 011101 (2008).

- [9] Y. Tanguy, T. Ackemann, W. J. Firth, and R. Jäger, *Phys. Rev. Lett.* **100**, 013907 (2008).
- [10] A. J. Scroggie, W. J. Firth, and G. L. Oppo, *Phys. Rev. A* **80**, 013829 (2009).
- [11] N. N. Rosanov and S. V. Fedorov, *Opt. Spectrosc.* **72**, 782 (1992).
- [12] A. G. Vladimirov, S. V. Fedorov, N. A. Kaliteevskii, G. V. Khodova, and N. N. Rosanov, *J. Opt. B* **1**, 101 (1999).
- [13] N. N. Rosanov, *Spatial Hysteresis and Optical Patterns* (Springer-Verlag, Berlin, 2002).
- [14] S. V. Fedorov, A. G. Vladimirov, G. V. Khodova, and N. N. Rosanov, *Phys. Rev. E* **61**, 5814 (2000).
- [15] M. Bache, F. Prati, G. Tissoni, R. Kheradmand, L. A. Lugiato, I. Protsenko, and M. Brambilla, *Appl. Phys. B* **81**, 913 (2005).
- [16] P. Genevet, S. Barland, M. Giudici, and J. R. Tredicce, *Phys. Rev. Lett.* **101**, 123905 (2008).
- [17] L. A. Lugiato, *IEEE J. Quantum Electron.* **39**, 193 (2003).
- [18] P. Genevet, S. Barland, M. Giudici, and J. R. Tredicce, *Phys. Rev. A* **79**, 033819 (2009).
- [19] F. Prati and L. Columbo, *Phys. Rev. A* **75**, 053811 (2007).
- [20] X. Hachair *et al.*, *J. Sel. Top. Quantum Electron.* **12**, 339 (2006).
- [21] W. W. Chow, S. W. Koch, and M. Sargent III, *Semiconductor Laser Physics* (Springer-Verlag, Berlin, 1994).
- [22] R. Lang and K. Kobayashi, *IEEE J. Quantum Electron.* **16**, 347 (1980).